



Spatial resolution enhancement of coherent Doppler wind lidar using joint time–frequency analysis



Chong Wang, Haiyun Xia ^{*}, Yanping Liu, Shengfu Lin, Xiankang Dou

School of Earth and Space Sciences, University of Science and Technology of China, Hefei, 230026, China

Key Laboratory of Geospace Environment, Chinese Academy of Sciences, Hefei, 230026, China

CAS Center for Excellence in Quantum Information and Quantum Physics, Hefei, 230026, China

ARTICLE INFO

Keywords:

Coherent Doppler wind lidar
Wind shear
Spatial resolution enhancement
Joint time–frequency analysis
Adaptive optimized kernel

ABSTRACT

Spatial resolution enhancement of a coherent detection Doppler wind lidar (CDWL) is generally achieved by reducing the pulse duration of the transmitted laser according to the basic lidar equation, inevitably, at sacrifice of other properties, such as the signal to noise ratio, maximum detection range and real time data processing. To solve this problem, a joint time–frequency analysis (JTFA) method is adopted in the CDWL. By comparing the performance of Cohen's class in analysis and wind retrieval simulation, the adaptive optimized kernel (AOK) is picked up as the best JTFA method in the CDWL. In experiment, wind profiles retrieved using the JTFA and the FFT are compared with the result simulated using the software ANSYS 18.0. Benefiting from the high spatial resolution of the JTFA method, the dynamic structure of wind shear in the gap of two tall buildings is detected clearly, which agrees well with the simulation.

1. Introduction

Doppler wind lidar (DWL) has been proved very useful in many fields, such as the aviation safety [1], wind power generation [2], weather forecast [3], air pollution monitoring [4] and scientific researches [5].

Remote sensing of wind using DWL with meter spatial resolution is still a challenge now. In some specific applications, wind detection with both long range and high spatial resolution are highly required. For example, tropical hurricanes have serious effects on human lives and property, but some phenomena remain unexplained. As one of the most effective methods for wind field remote sensing, DWL with high spatial resolution can make remote sensing of the hurricane and provide the dynamic structure in the boundary layer near and in its supercell, which has a radius about 100 m [6]. In air-transportation industry, the Doppler wind lidar can be used to enhance the aviation safety by detecting the aircraft wake vortices and wind shear in the runway. However, the aircraft wake vortices are small-scale phenomena, since the wingspan of the aircraft is tens of meters [7].

Benefiting from the development of optical fiber communication, DWL at 1.5 μm is developed rapidly in recent years [8]. Doppler wind lidar can be divided into direct detection Doppler wind lidar (DDWL) and coherent detection Doppler wind lidar (CDWL). Recently, CDWL is developed intensively around the world, with a spatial resolution

ranging from 15 to 100 m, as list in Table 1. Obviously, spatial resolution is not high enough to study the phenomena mentioned above.

2. Principle

The transmitted laser pulse from a lidar can be represented as :

$$P_T(t) = \exp[-4 \ln(2)t^2 / \Delta T^2]. \quad (1)$$

The spatial resolution ΔR is determined by the pulse duration ΔT (FWHM) as:

$$\Delta R = c\Delta T / 2, \quad (2)$$

where c is the speed of light in the atmosphere. Intuitively, to enhance the spatial resolution, one should use laser source with shorter pulse duration. In the DDWL scheme, the frequency discriminator should be optimized according to this change [18–20]. Recently, a spatial resolution of 10 m is achieved [21].

In the CDWL, a shorter laser pulse will decrease the signal to noise ratio, resulting decaying detection range and poor precision of wind velocity. The reasons are as follows:

Firstly, in the CDWL, the wind velocity is retrieved from the backscatter power spectrum, as shown in Fig. 1(a), the red line is a typical power

^{*} Corresponding author.

E-mail address: hsia@ustc.edu.cn (H. Xia).

Table 1
The spatial resolution of some CDWLs.

Research group	Pulse energy	Spatial resolution	Max distance
NASA [9]	35 μJ	15 m	–
Lockheed-Martin [10]	2500 μJ	100 m	15 km
LEOSPHERE [11]	120 μJ	30 m	6 km
ONERA [12]	120 μJ	30 m	1.2 km
Mitsubishi [13]	500 μJ	50 m	4.2 km
SIOM [14]	43 μJ	75 m	3 km
BIT [15]	43 μJ	75 m	3 km
OUC [16]	100 μJ	30 m	3 km
USTC [17]	100 μJ	45 m	6 km

spectrum with noise. Given a Gaussian transform-limited laser pulse, the width of its power spectrum width Δf (FWHM) is inversely proportional to ΔT as: [22]

$$\Delta f = \frac{\sqrt{\ln(2)}}{\sqrt{2\pi}\Delta T}. \quad (3)$$

Fig. 1(a) shows simulated power spectra with ΔT changing from 300 to 10 ns, with a modulated frequency shift of $\Delta\nu = 80$ MHz and wind velocity of -10 m/s. As shown in the figure, a shorter ΔT will broaden its corresponding Δf , which may finally induce a crosstalk between the spectra of local oscillator and that of the backscattering, as shown as the green dash line with $\Delta T = 10$ ns. The crosstalk makes the wind velocity hard to be retrieved. In order to resolve this problem, a larger modulated frequency shift should be implemented. As shown in Fig. 1(b), with $\Delta\nu = 240$ MHz, the crosstalk can be mitigated. But according to Nyquist–Shannon sampling theorem, this means the ADC should have higher sampling rate and the amount of raw data will be increased substantially.

Secondly, SNR is proportional to ΔT . With an assumption of a matched filter, the detection bandwidth can be expressed as $B = 1/\Delta T$ [23]. The SNR equation of the CDWL is derived as:

$$SNR(R) = \frac{\eta_o \eta_h \lambda U_T \beta T_r^2(R) \pi D^2 \Delta T}{8hR^2}, \quad (4)$$

where η_o is the total optical efficiency, η_h is the heterodyne efficiency, λ is the wavelength, U_T is the transmitted laser energy, β is the atmospheric backscatter coefficient, $T_r(R)$ is the single-way atmospheric transmittance, D is the effective aperture diameter of the telescope, h is the Planck constant. A laser pulse with shorter duration ΔT will decrease the SNR obviously.

In a CDWL, the raw signal is non-stationary, the spatial resolution and range bin information is retrieved by time-of-flight method in the time domain. The Doppler frequency shift induced by wind is retrieved using Fast Fourier transform (FFT) or other algorithms [24–27] in the frequency domain. Such a signal processing method usually describes how the spectra change with time. On the contrary, Joint time–frequency analysis (JTFA) is a versatile data processing method, expressing the signal in a time–frequency distribution [28]. There are many successful applications using the JTFA, such as earthquake research [29], the structural health monitoring [30], the 4G LTE signal processing [31] and Radar [32]. JTFA improves the spatial resolution and reduces the noise. There are many different JTFA methods, but not every JTFA method is suitable for data processing in practical CDWL [33].

Cohen’s class is one of the most important members in JTFA, and can be expressed as the 2-D Fourier transform of a weighted ambiguity function of the signal under analysis: [34]

$$P(t, \omega) = \frac{1}{4\pi^2} \int_{-\infty}^{+\infty} \int_{-\infty}^{+\infty} A(\theta, \tau) \exp(-j\theta t - j\tau\omega) \phi(\theta, \tau) d\theta d\tau, \quad (5)$$

$A(\theta, \tau)$ is a symmetrical AF expressed as:

$$A(\theta, \tau) = \int_{-\infty}^{+\infty} s(t + \frac{\tau}{2}) s^*(t - \frac{\tau}{2}) \exp(j\theta t) dt, \quad (6)$$

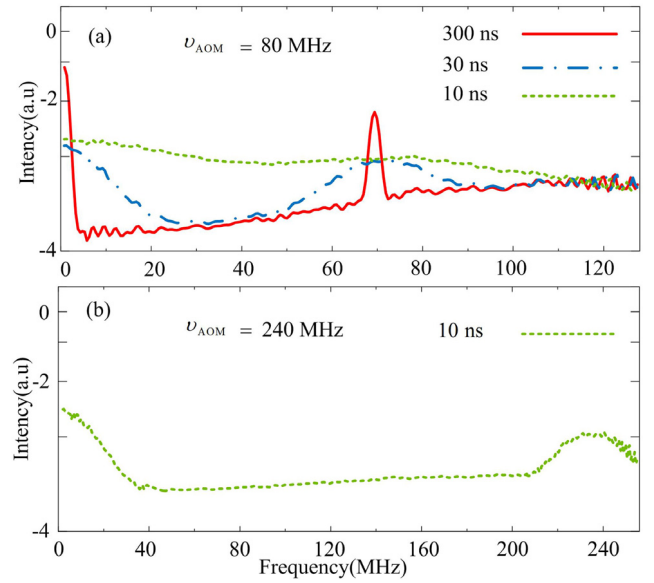


Fig. 1. (a) Power spectra with $v_{AOM} = 80$ MHz, $\Delta T = 300$ ns (red line), $\Delta T = 30$ ns (dot dash line), $\Delta T = 10$ ns (green dashed line); (b) Power spectrum with $v_{AOM} = 240$ MHz, $\Delta T = 10$ ns.

Table 2
Kernel functions for some Cohen’s class.

Representation	Kernel $\phi(\theta, \tau)$
Wigner–Ville (WVD)	1
Spectrogram(SP)	$\int_{-\infty}^{+\infty} h^*(u - \tau/2) h(u + \tau/2) \exp(-j\theta u) du$
Adaptive Optimal Kernel (AOK)	$\exp\{-\theta^2 + \tau^2\} / [2\sigma^2 \arctan(\tau/\theta)]$

$s(t)$ is analytical expression of the real signal and is defined as:

$$s(t) = s_r(t) + jHT[s_r(t)], \quad (7)$$

where $s_r(t)$ is the real signal and $HT[s_r(t)]$ is the Hilbert Transform of $s_r(t)$. $\phi(\theta, \tau)$ is the kernel function, which is independent of time and frequency. In Cohen’s class, the only difference between the algorithms is their kernel function. For example, Wigner–Ville distribution (WVD) is the basic function in Cohen’s class, but suffers from inherent cross-term contamination, making the useful information hard to be extracted. By using different kernel window functions, the interference can be mitigated significantly. As an example, three kernel functions in Cohen’s class are listed in Table 2.

In the FFT, the WVD or the spectrogram (SP) methods, all the parameters in its kernel function is fixed. But the adaptive optimal kernel will optimize its parameters to match the signal as it changing. In the case of non-stationary signal processing, the JTFA with AOK method can extract the signal and suppress both the noise and inherent cross-term contamination effectively.

In the case of a stationary signal, its power spectral density is the Fourier transform of its auto-correlation function. For a non-stationary signal $x(t)$, this relationship still holds. The time-dependent power spectral density of $x(t)$ called Winger distribution is written as:

$$W_x(t, \omega) = \int_{-\infty}^{+\infty} R_x(t, \tau) \exp(-j2\pi\omega\tau) d\tau, \quad (8)$$

where,

$$R_x(t, \tau) = x(t + \tau/2) x^*(t - \tau/2), \quad (9)$$

where x^* is the conjugation of x . Eq. (8) is the Fourier transform of Eq. (9). If the Fourier transform of Eq. (9) is taken with respect to t instead of τ , the ambiguity function can be derived as:

$$A_x(\theta, \tau) = \int_{-\infty}^{+\infty} x(t + \tau/2) x^*(t - \tau/2) \exp(-j2\pi t\theta) dt. \quad (10)$$

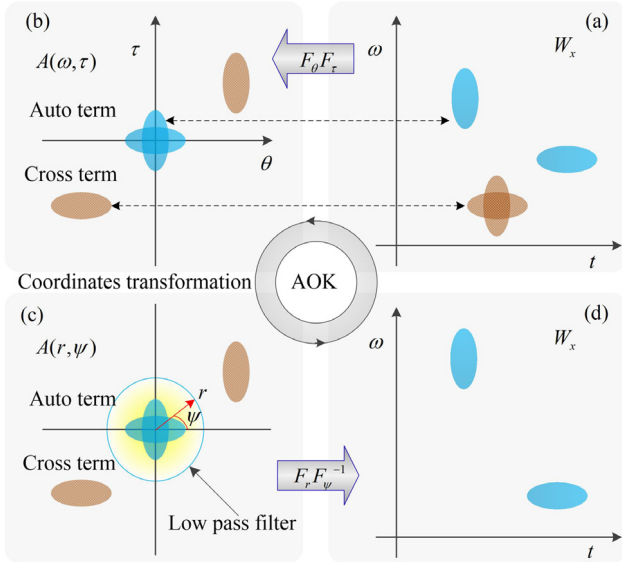


Fig. 2. (a) and (b) are the demonstration of the auto term and cross term of a non-stationary signal in the Winger distribution and the ambiguity distribution. (c) and (d) are the ambiguity function with a low pass filter in polar coordinates and the result of the AOK.

The benefit of this transform can be seen from Fig. 2(a) and (b). In the Winger distribution, the locations of auto term and cross term are unpredicted, but in the ambiguity distribution, the auto term is located near the origin and the cross term is deviated from the origin. Therefore, with an appropriate filter function, the cross term noise can be filtered out.

In the AOK method, the optimal kernel is adapted to a signal by solving the following optimization problem: [35,36]

$$\phi_{opt} = \max_{\phi} \int_0^{2\pi} \int_0^{+\infty} |A(r, \psi)\phi(r, \psi)|^2 r dr d\psi, \quad (11)$$

subject to the kernel function, which is a 2-D Gaussian function defined as:

$$\phi(r, \psi) = \exp[-r^2/2\sigma^2(\psi)], \quad (12)$$

$$\begin{aligned} & \frac{1}{4\pi^2} \int_0^{2\pi} \int_0^{\infty} |\phi(r, \psi)|^2 r dr d\psi \\ & = \frac{1}{4\pi^2} \int_0^{2\pi} \sigma^2(\psi) d\psi \leq \alpha, \alpha \geq 0, \end{aligned} \quad (13)$$

where $r = \sqrt{\theta^2 + \tau^2}$, $\psi = \arctan(\tau/\theta)$, $\sigma(\psi)$ controls the spread of the Gaussian function, or the projecting area in the ambiguity function distribution, as shown in the cyan circle in Fig. 2(c).

Eq. (12) sets the window of the kernel as a Gaussian function, which is a low pass filter. Eq. (13) limits the volume of the kernel to α , as shown in Fig. 2(c), if the α is too large, the cross term noise will be involved in the signal, inversely, if the α is too small, useful auto term will be filtered out. Generally, $0 \leq \alpha \leq 5$ ($\alpha = 1$ is used in this work). The optimal AOK will make Eq. (11) get the maximum value. The procedure to solve the Eqs. (11) to (13) is shown in the Appendix.

3. Simulation

The optic layout of the CDWL is shown in Fig. 3, the seed laser emits a CW laser, the beam splitter divides the laser into local oscillator and transmitted laser. The continuous transmitted laser is chopped into a pulse train with a frequency shift of 80 MHz and 300 ns pulse duration by using an acoustic-optical modulator (AOM). Going through

Table 3
Key specifications of CDWL.

Parameter	Value
Winger-Ville (WVD)	1
Wavelength (nm)	1548.1
Pulse energy (μ J)	100
Pulse duration (ns)	300
Pulse rate (Hz)	15 625
LO power (mW)	1
AOM (MHz)	80
Diameter (mm)	80
ADC rate (MHz)	250

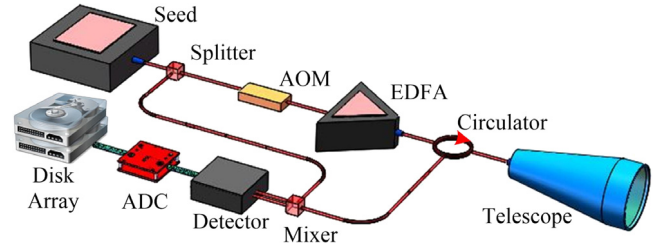


Fig. 3. Optic layout of the CDWL.

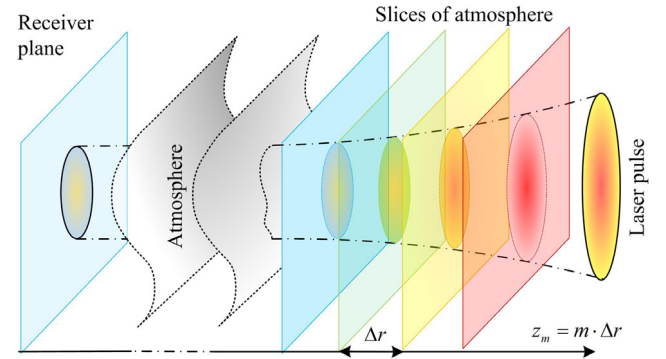


Fig. 4. Schematic of the Feuilleté model.

an erbium doped fiber amplifier (EDFA), the laser is amplified with a pulse energy of 100 μ J. Then, the pulse passing through the circulator is collimated and sent to the atmosphere by a telescope. The backscattering photons are collected by the same telescope and finally mixed with local oscillator in the 3 dB coupler (mixer). Then, the mixed signal is measured by the balanced detector and digitalized by an ADC. The raw data is transformed into two parts, one is processed in real-time by the digital signal processors (DSP) with the FFT, and the other is stored in a disk array for postprocessing.

In order to compare the performance of the FFT, the WVD, the SP and the JTFA with AOK, a CDWL signal is simulated and processed.

According to Feuilleté model [37], the detection signal over M slices is simulated as:

$$\begin{aligned} S(t) = & 2(P_{LO})^{1/2} \exp(j2\pi v_{IF}t) \sum_M [P_T(t - 2m\Delta r/c)]^{1/2} \\ & \times \exp[j\varphi(t - 2m\Delta r/c)] \tilde{\kappa}_m(t) \exp(-j2\pi v_m t/\lambda), \end{aligned} \quad (14)$$

where m is the index number of slices, Δr is the range interval between two slices, P_{LO} is the power of local oscillator, v_{IF} is the intermediate frequency, φ is a phase function, $\tilde{\kappa}_m$ is a circular random variable, v_m is the Doppler shift in the m th slice. The parameters used in the simulation are list in Table 3, the schematic of the Feuilleté model is shown in Fig. 4.

In order to evaluate the performance of spatial resolution in different methods, wind shears are added in the simulation. Fig. 5(a) shows the

simulated raw CDWL signal from 0 to 3 km in logarithmic coordinates. The simulated wind velocity distribution is shown in Fig. 5(b) with the red line. The wind velocity distribution retrieved by the FFT is plotted as circles in Fig. 5(b), the raw data points for the FFT are 100 and the spatial resolution is 60 m as one range bin. The retrieved wind velocity along distance agrees well with the preset value, but the detail of wind shear is smoothed and cannot be distinguished due to the low spatial resolution. Fig. 5(c) shows the result processed by the WVD, the minimum spatial resolution is set to 0.6 m. Due to the cross-term contamination, the wind velocity is hard to be retrieved. Fig. 5(d) is the result processed by the SP, the minimum spatial resolution is set to 6 m and the black line is the connection of maximum peaks. Fig. 5(e) is the result processed by the JTFA with AOK, the minimum spatial resolution is set to 1.2 m and the black line is the connection of maximum peaks. Comparing with FFT and SP, the AOK improves the spatial resolution, the detail of wind shear can be seen clearly, especially at 1.5 km, as the preset velocity changing dramatically, the result of the JTFA changes immediately without any ambiguity. JTFA has better spatial resolution and agrees with the simulated velocity better. Comparing with the WVD, the interference is significantly mitigated. According to the uncertainty principle, a perfect resolution in time and frequency cannot be obtained simultaneously. In fact, the popular kernels, including wavelet transform, Choi–Williams distribution, Born–Jordan distribution and reduced interference distribution are tested, only four typical data processing methods like the FFT, the WVD, the SP and the JTFA with AOK are shown, with a compromise of high spatial resolution and mitigation of interference. The AOK is chosen as the optimal JTFA in this work.

4. Experiment

Wind velocity detection is carried out at Hefei (31.83°N, 117.25°E) in Anhui province, China, started at 00:30 on Mar. 18, 2017. The location is 54 m above the ground. The accuracy and stability of the CDWL has been demonstrated earlier [17]. Before the experiment, a wind field simulation is carried out to find a small-scale wind shear. By enhancing the spatial resolution of CDWL using JTFA, one will see the dynamic structure of wind shear in detail.

In the simulation, according to the actual buildings' location and the topographic map from Google, a standard $k-\epsilon$ model is built for finite element analysis [38,39]. The input velocity is 1 m/s (which is measured by a ultrasonic wind sensor Vaisala windcap WMT52) towards the north at the high of 54 m. The velocity distribution uses equation:

$$v(z)/v_b = (z/z_b)^r, \quad (15)$$

where v_b and z_b are reference speed and height, respectively; r is the ground roughness index. According to the reference, a class C landscape types with $r = 0.22$ is set. A wind shear is found between two buildings 1.1 km far away in the north. The simulated model and wind field is shown in Fig. 6. The simulation shows that the air flow is restricted and accelerated in the gap between two tall buildings.

In the experiment, the laser beam goes through the gap between two tall buildings 1.1 km away, as shown in Fig. 6. Two data processing methods are implemented for comparison. A radial wind velocity distribution is shown in Fig. 7(a). The red circles are the result of the FFT, the temporal and spatial resolution is 2 s and 60 m, respectively. The black line is the result of the JTFA, the temporal and spatial resolution is 2 s and 1.2 m, respectively. A wind shear can be seen at the distance of 1.1 km, in order to see the detail of the wind shear, an enlarged radial wind velocity profile from 0.92 to 1.22 km is plotted in Fig. 7(b). It is hard to image the dynamic structure of the wind shear by using the FFT results due to its poor spatial resolution. In contrast, the dynamic structure can be detected using the JTFA clearly, which is in good agreement with the simulation.

To test the accuracy and stability of the JTFA based on AOK method, 20 sets of wind velocity profiles within 4 s are retrieved, where the

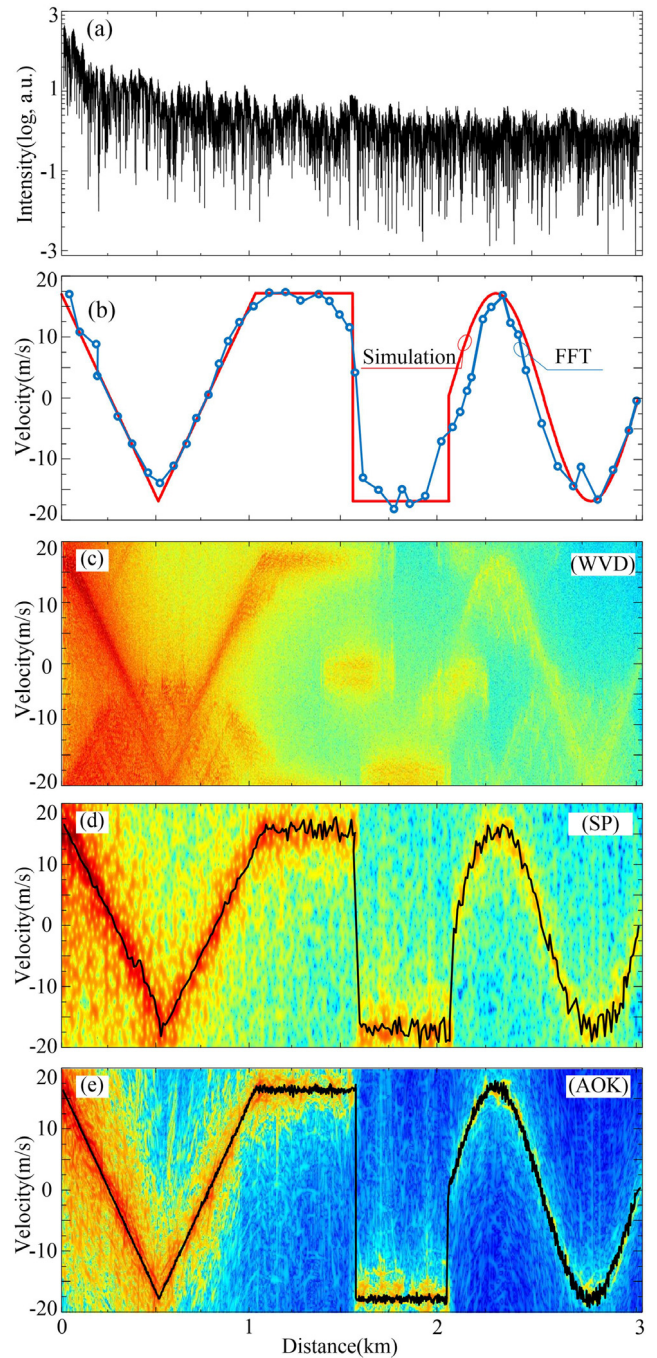


Fig. 5. (a) Simulated time-domain CDWL signal; (b) Simulated wind velocity distribution and the result processed by the FFT; (c) Result processed by the WVD; (d) Result processed by the SP; (e) Result processed by the JTFA with AOK.

temporal and spatial resolution is 0.2 s and 1.2 m, take the advantage of high signal to noise ratio in the near field detection. The results are shown in Fig. 8(a). Supposing the wind velocity in the line of sight is stable within the detection period, a stationary wind shear profile in the gap of buildings should be monitored. A histogram of the differences between the averaged profile within 4 s and the wind value at each point is plotted as Fig. 8(b). The mean velocity difference is nearly 0 m/s and the standard deviation is 0.09 m/s, indicating a high stability of the JTFA method.

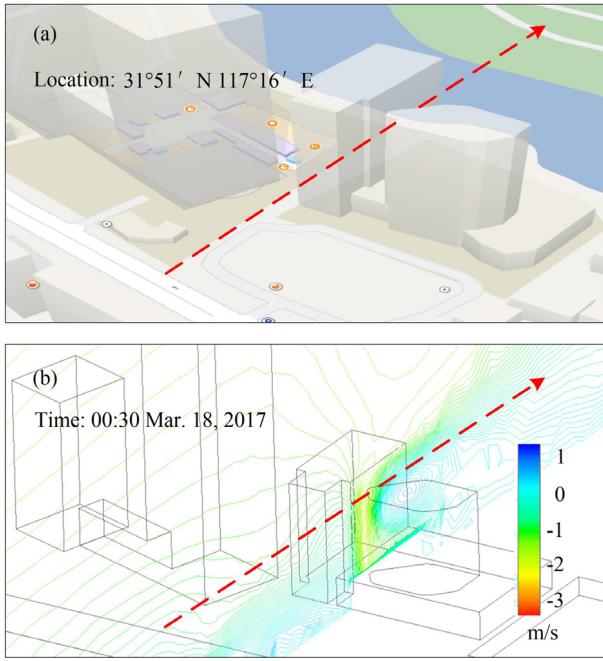


Fig. 6. (a) 3D Google map of the location, the red line represents the laser beam; (b) Simulated wind field in the gap of two tall buildings.

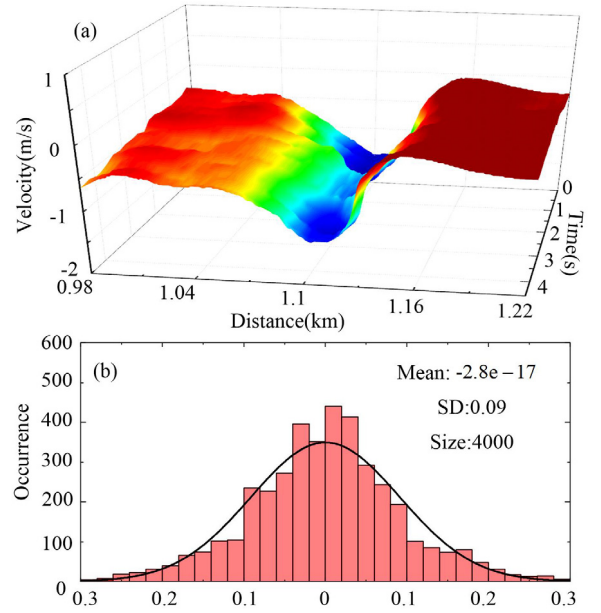


Fig. 8. (a) 20 sets of wind velocity distribution near the wind shear location in 4 s. (b) A histogram of the differences between the averaged profile in 4 s and the wind value at each point.

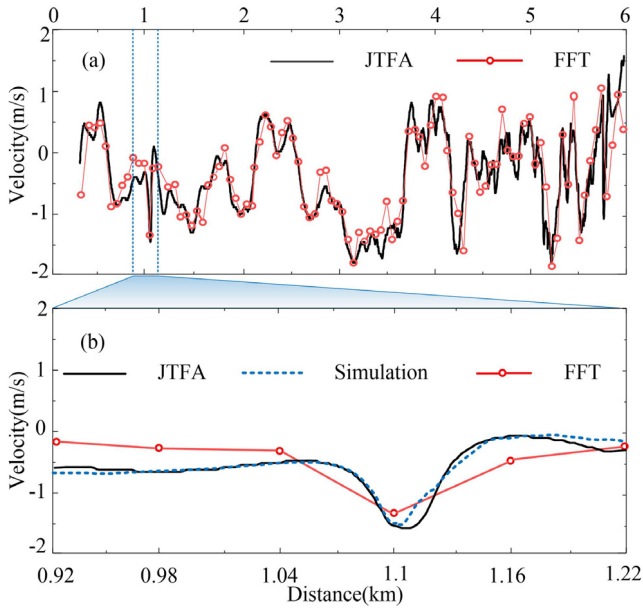


Fig. 7. (a) Radial wind velocity distribution processed by the FFT and the JTFA, the spatial resolution is 60 m and 1.2 m, respectively; (b) Detail of wind shear induced by two high buildings at the distance of 1.1 km. The black line is the result of the JTFA, the red circles are the result of the FFT and the dashed blue line is the result of simulation.

5. Conclusion

A CDWL using JTFA is demonstrated. A simulated time-domain CDWL signal with wind shear is generated, and processed by using the FFT, the WVD, the SP and the JTFA with AOK. The JTFA has shown its advantages with high spatial resolution, high aggregation and low inherent cross-term contamination. During the real wind velocity detection, JTFA-AOK and FFT are implemented and compared. A good agreement between the JTFA and wind field simulation in the gap of

two tall buildings shows the stability and accuracy of the JTFA. Taking advantage of the high spatial and temporal resolutions of the JTFA, this will be useful in many fields, such as the detection of aircraft wake turbulence, wind turbine vortex or wind tunnel.

Appendix

Gradient Ascent Algorithm is proposed by Richard G. Baraniuk and Douglas L. Jones to solve Eqs. (11) to (13). A short review is introduced [33]:

Discrete Eqs. (11) to (13) as:

$$\phi_p(p, q) = \exp\left[-\frac{(p\Delta r)^2}{2\sigma_q^2(q\Delta\psi)}\right], \quad (\text{A.1})$$

$$p = 0, \dots, P-1, q = 0, \dots, Q-1,$$

$$\frac{\Delta\psi}{2\pi} \sum_{q=0}^{Q-1} \sigma_q^2 \leq \alpha, \quad (\text{A.2})$$

$$\sigma_q = \sigma(q\Delta\psi), \quad (\text{A.3})$$

p and q are the radius and angle indices, Δr and $\Delta\psi$ are the step sizes of radius and angle. Iterate the $\underline{\sigma}$ with:

$$\underline{\sigma}(k+1) = \underline{\sigma}(k) + \mu \nabla_{\underline{\sigma}}(K), \quad (\text{A.4})$$

where:

$$\nabla_q(k) = \frac{\Delta r^4 \Delta\psi}{\sigma_q^3(k)} \sum_{p=1}^{P-1} p^3 |A_p(p, q)| \exp\left[-\frac{(p\Delta r)^2}{\sigma_q^2(k)}\right], \quad (\text{A.5})$$

$$q = 0, \dots, Q-1,$$

μ is a positive constant small enough to ensure the stability of the iterations. The initial condition is:

$$\underline{\sigma}(0) = \sqrt{\frac{2\pi\alpha}{Q\Delta\psi}} [1, \dots, 1]^T. \quad (\text{A.6})$$

Because $\nabla_q(k) \geq 0$, $\underline{\sigma}$ will be increased after each iteration, in order to satisfy the constrain of Eq. (13), $\underline{\sigma}$ will be normalized after each iteration

with:

$$\underline{\sigma}(k+1) = \underline{\sigma}(k+1) \sqrt{\frac{2\pi\alpha}{\Delta\psi \sum_q \sigma_q^2(k+1)}}. \quad (\text{A.7})$$

The iteration is terminated once Eq. (11) gets the maximum value. The matlab program is provided out by Douglas L. Jones and Tony Reina at:

https://cn.mathworks.com/matlabcentral/fileexchange/13869-adaptive-optimal-kernel?s_tid=gn_loc_drop.

References

- [1] Hamaki Inokuchi, T. Hisamichi, A. Toshiyuki, Development of an onboard Doppler lidar for flight safety, *J. Aircr.* 46 (2009) 1411.
- [2] G. Giebel, R. Brownsword, G. Kariniotakis, M. Denhard, C. Draxl, The state-of-the-art in short-term prediction of wind power: A literature overview. ANEMOS. plus, 2011.
- [3] E.B. Wayman, D.E. George, R. Franklin, M.A. Robert, E.M. John, A.B. David, P. Jan, R.M. Hardesty, J.P. Madison, T.M. Robert, T.N. Krishnamurti, A.B. Robert, R.A. John, C.L. Andrew, M. James, Lidar-measured winds from space: a key component for weather and climate prediction, *Bull. Am. Meteorol. Soc.* 76 (1995) 869.
- [4] J. Zhang, Z. Chen, Y. Lu, H. Gui, J. Liu, W. Liu, J. Wang, T. Yu, Y. Cheng, Y. Chen, B. Ge, Y. Fan, X. Luo, Characteristics of aerosol size distribution and vertical backscattering coefficient profile during 2014 APEC in Beijing, *Atmos. Environ.* 148 (2017) 30.
- [5] B. Witschas, S. Rahm, A. Dörnbrack, J. Wagner, M. Rapp, Airborne wind lidar measurements of vertical and horizontal winds for the investigation of orographically induced gravity waves, *J. Atmos. Ocean. Technol.* 34 (2017) 1371.
- [6] H.B. Bluestein, J.B. Houser, M.M. French, J.C. Snyder, G.D. Emmitt, I. PopStefanija, C. Baldi, R.T. Bluth, Observations of the boundary layer near tornadoes and in supercells using a mobile, collocated, pulsed doppler lidar and radar, *J. Atmos. Ocean. Technol.* 31 (2014) 302.
- [7] I.N. Smalikho, V.A. Banakh, Estimation of aircraft wake vortex parameters from data measured with a 1.5- μm coherent doppler lidar, *Opt. Lett.* 40 (2015) 3408.
- [8] S. Kameyama, T. Yanagisawa, T. Ando, T. Sakimura, H. Tanaka, M. Furuta, Y. Hirano, Development of wind sensing coherent Doppler LIDAR at mitsubishi electric corporation-from late 1990s to 2013, in: Proceedings of 17th Coherent Laser Radar Conference, Barcelona, Spain, 2013.
- [9] N.S. Prasad, R. Sibell, S. Vitorino, R. Higgins, A. Tracy, An all-fiber, modular, compact wind lidar for wind sensing and wake vortex applications, in: SPIE Defense + Security, International Society for Optics and Photonics, 2015, p. 94650C-1.
- [10] M. Weissmann, A. Dörnbrack, J.D. Doyle, Vorticity from line-of-sight lidar velocity scans, *J. Atmos. Ocean. Technol.* 26 (2009) 2683.
- [11] T. Mikkelsen, Lidar-based research and innovation at DTU wind energy—a review, *J. Phys.* 524 (2014) 012007.
- [12] A. Dolfi-Bouteyre, G. Canat, M. Valla, B. Augere, C. Besson, D. Goular, L. Lombard, J.P. Cariou, A. Durecu, D. Fleury, L. Bricteux, S. Brousmitche, S. Lugan, B. Macq, Pulsed 1.5- μm LIDAR for axial aircraft wake vortex detection based on high-brightness large-core fiber amplifier, *IEEE. J. Sel. Top. Quantum* 15 (2009) 441.
- [13] A. Yagi, A. Inagaki, M. Kanda, C. Fujiwara, Y. Fujiyoshi, Nature of streaky structures observed with a doppler lidar, *Bound.-Layer Meteorol.* 163 (2017) 19.
- [14] W. Diao, X. Zhang, J. Liu, X. Zhu, Y. Liu, D. Bi, W. Chen, All fiber pulsed coherent lidar development for wind profiles measurements in boundary layers, *Chin. Opt. Lett.* 12 (2014) 072801.
- [15] Z. Bu, Y. Zhang, S. Chen, G. Pan, L. Li, H. Chen, Noise modeling by the trend of each range gate for coherent doppler LIDAR, *Opt. Eng.* 53 (2014) 063109.
- [16] X. Zhai, S. Wu, B. Liu, Doppler lidar investigation of wind turbine wake characteristics and atmospheric turbulence under different surface roughness, *Opt. Express* 25 (2017) A515.
- [17] C. Wang, H. Xia, M. Shangguan, Y. Wu, L. Wang, J. Qiu, R. Zhang, 1.5 μm polarization coherent lidar incorporating time-division multiplexing, *Opt. Express* 25 (2012) 20663.
- [18] H. Xia, X. Dou, D. Sun, Z. Shu, X. Xue, Y. Han, D. Hu, Y. Han, T. Chen, Mid-altitude wind measurements with mobile rayleigh doppler lidar incorporating systemlevel optical frequency control method, *Opt. Express* 20 (2012) 15286.
- [19] J. Qiu, H. Xia, X. Dou, M. Shangguan, C. Wang, Y. Zhang, Optimization of scanning Fabry–Perot interferometer in the high spectral resolution lidar for stratospheric temperature detection, *Opt. Eng.* 55 (2016) 084107.
- [20] H. Xia, M. Shangguan, R. Zhao, Y. Han, Z. Shu, X. Xue, Y. Han, C. Wang, J. Qiu, Stratospheric temperature measurement with scanning Fabry–Perot interferometer for wind retrieval from mobile Rayleigh Doppler lidar, *Opt. Express* 22 (2014) 21775.
- [21] M. Shangguan, H. Xia, C. Wang, J. Qiu, S. Lin, X. Dou, Q. Zhang, J. Pan, Dual-frequency doppler lidar for wind detection with a superconducting nanowire single-photon detector, *Opt. Lett.* 42 (2017) 3541.
- [22] R. Frehlich, M. Yadlowsky, Performance of mean-frequency estimators for Doppler radar and lidar, *J. Atmos. Ocean. Technol.* 11 (1994) 1217.
- [23] R. Frehlich, M. Kavaya, Coherent laser radar performance for general atmospheric refractive turbulence, *Appl. Opt.* 30 (1991) 5325.
- [24] S. Kameyama, T. Ando, K. Asaka, Y. Hirano, S. Wadaka, Performance of discrete-Fourier-transform-based velocity estimators for a wind-sensing coherent doppler lidar system in the kolmogorov turbulence regime, *IEEE Trans. Geosci. Remote* 47 (2009) 3560.
- [25] S. Abeysekera, Performance of pulse-pair method of doppler estimation, *IEEE Aerosp. Electron Syst.* 34 (1998) 520.
- [26] M. Levin, Power spectrum parameter estimation, *IEEE Trans. Inform. Theory* 11 (1965) 100.
- [27] M. Shirakawa, D. Zmic, The probability density of a maximum likelihood mean frequency estimator, *IEEE Trans. Acoust. Speech Signal Process.* 31 (1983) 1197.
- [28] L. Cohen, Time-frequency distributions—a review, *Proc. IEEE* 77 (1989) 941.
- [29] R. Stockwell, L. Mansinha, R. Lowe, Localization of the complex spectrum: the S transform, *IEEE Trans. Signal Process.* 44 (1996) 998.
- [30] A. Raghavan, C. Cesnik, Review of guided-wave structural health monitoring, *Shock Vib. Dig.* 39 (2007) 91.
- [31] L. Dai, Z. Wang, Z. Yang, Spectrally efficient time–frequency training OFDM for mobile large-scale MIMO systems, *IEEE J. Sel. Areas Commun.* 31 (2013) 251.
- [32] V. Chen, S. Qian, Joint time–frequency transform for radar range-doppler imaging, *IEEE Trans. Aerosp. Electron. Syst.* 34 (1998) 486.
- [33] S. Barbarossa, A. Farina, Detection and imaging of moving objects with synthetic aperture radar. Part 2: Joint time–frequency analysis by Wigner-Ville distribution, *IEEE Proc. F* 139 (1992) 89.
- [34] D. Jones, R. Baraniuk, An adaptive optimal-kernel time–frequency representation, *IEEE Trans. Signal Process.* 40 (1995) 2361.
- [35] R. Baraniuk, D. Jones, A radially-Gaussian, signal-dependent time–frequency representation, in: 1991 International Conference on Acoustics, Speech, and Signal Processing, 1991, ICASSP-91, IEEE, 1991, p. 3181.
- [36] R. Baraniuk, D. Jones, Signal-dependent time–frequency analysis using a radially Gaussian kernel, *IEEE Trans. Signal Process.* 23 (1993) 263.
- [37] P. Salamitou, A. Dabas, P. Flamant, Simulation in the time domain for heterodyne coherent laser radar, *Appl. Opt.* 34 (1995) 499.
- [38] W. He, W. Yuan, Numerical simulation of wind field characteristics around two adjacent high-rise buildings, *J. Appl. Math. Phys.* 2 (2014) 264.
- [39] L. Lu, K. Ip, Investigation on the feasibility and enhancement methods of wind power utilization in high-rise buildings of Hong Kong, *Renew. Sustainable Energy Rev.* 13 (2009) 450.